In Situ Observations of Kelvin–Helmholtz Waves along a Frontal Inversion

JOHN W. NIELSEN*

Department of Atmospheric Science, State University of New York at Albany, Albany, New York

(Manuscript received 31 December 1990, in final form 14 June 1991)

ABSTRACT

An unusual set of observations of amplifying Kelvin–Helmholtz waves along a New England coastal front inversion is presented and compared to linear theory. The waves were observed by instrumented aircraft traversing the coastal front at various levels and measuring temperature and horizontal and vertical wind components at one-second intervals. The most prominent group of waves had amplitudes in the neighborhood of 100 m, comparable to the total depth of the inversion, and wavelengths near 1.7 km. Spectral analysis of data from an aircraft pass located just above the inversion indicates that Kelvin–Helmholtz billows of 1–2-km wavelength were present over a distance of at least 25 km.

Numerical solution of the Taylor–Goldstein equation for observed and specified basic-state vertical profiles confirms that instability of the Kelvin–Helmholtz type is the dominant mode of instability. The wavelength of the most unstable mode is found to be strongly sensitive to the relative thicknesses of the shear and inversion layers.

The observed waves illustrate a mechanism by which dammed cold air is eroded and accelerated toward the mountains, particularly as the ambient onshore wind increases or the cold air warms.

1. Introduction

The purpose of this paper is to document the morphology and dynamics of a set of waves observed along a New England coastal front inversion during the New England Winter Storms Experiment (NEWSEX). The waves were encountered by an instrumented aircraft making horizontal traverses within the lower troposphere normal to the surface frontal position. The data from a portion of one of the traverses include remarkably regular high-amplitude oscillations of temperature and wind, which we will demonstrate possess the characteristics of amplifying Kelvin–Helmholtz waves. The case is of interest both as a set of in situ wave observations and for its implications to the dynamics, modeling, and forecasting of cold-air damming and similar atmospheric flows.

Previously published observations of Kelvin–Helmholtz waves in the atmosphere have primarily consisted of visual observations of cloud signatures or detection of billow patterns using ground-based radar (for a review, see Fritts and Rastogi 1985). Direct observations of Kelvin–Helmholtz billows using instrumented aircraft have been fewer in number. Many such observations were taken during the early 1970s in connection with the phenomenon of clear-air turbulence (e.g., Axford 1973; Browning et al. 1973; Hardy et al. 1973; Metcalf and Atlas 1972). Of these, the flight-level observations most closely resembling the present case were those by Axford, who examined aircraft data from a horizontal traverse through a slightly sloping tropopause inversion and found 2.4-km wavelength excursions of temperature and wind to values characteristic of air above and below the inversion. More recent direct measurements have tended to concentrate on boundary-layer phenomena, utilizing either aircraft or tower observing systems (Busack and Brummer 1988; De Baas and Driedonks 1985; Merrill 1977). These recent studies have included linear stability analyses of the observed basic states, and all have found dominant unstable modes (of either the Kelvin–Helmholtz or resonant gravity wave type) closely matching the observed waves.

The waves that are the subject of the present case study occurred on 4 December 1983. These waves were the most prominent of any observed by aircraft during NEWSEX. The mesoscale structure of the coastal front along which the waves were found has been examined by Nielsen (1989) and Nielsen and Neilley (1990, hereafter referred to as NiNe). Like other coastal fronts studied by NiNe, the 4 December 1983 front took the form of a density current oriented approximately parallel to both the coastline and the inland orography. Strong Kelvin–Helmholtz instability and turbulent mixing is known to occur near the leading edge of laboratory and atmospheric density currents, including coastal fronts (Britter and Simpson 1978; Droegemeier and Wilhelmson 1987; Young and Johnson 1984;

* Current affiliation: Dept. of Meteorology, Texas A&M University.

Corresponding author address: Dr. John W. Nielsen, Dept. of Meteorology, Texas A&M University, College Station, TX 77843-3150.

NiNe), and such mixing was also observed in this case. However, this localized region of rapid mixing will not be the main focus of interest. Rather, we shall discuss waves that were observed along the coastal front/cold-air damming inversion primarily between 30 and 45 km behind the leading edge of the coastal front.

In section 2 we describe the dataset and its limitations, review the Taylor–Goldstein equation and the associated polarization relations, and discuss the method of solution of the linear instability eigenvalue problem. The observations of the waves are presented in section 3, and such quantities as wavelength, amplitude, phase speed, critical level, and regions of propagation and evanescence are estimated. In section 4 the instability characteristics of the observed basic state are examined. Because vertical profiles are not available simultaneous with the waves, a variety of observed and analytic profiles are used to explore the sensitivity of the instability characteristics to possible variations in the vertical structure of the basic state. Having established the basic instability mechanism of the observed flow as of the Kelvin–Helmholtz type, we proceed in section 5 to examine the data for expected signatures of breaking Kelvin–Helmholtz billows. The characteristics of this case are compared with the other NEWSEX coastal front cases in section 6. The data and theory are synthesized in the form of a two-dimensional depiction of the observed waves in section 7, and various implications of the observations are discussed.

2. Data and methods

a. The transformation of the aircraft data

This study uses temperature and wind data from the NCAR King Air instrumented aircraft. The three-dimensional wind data were determined by the INS (inertial navigation system) and airspeed sensors of the aircraft. This wind data has a relative accuracy of better than 0.1 m s^{-1} for variations in wind of two minutes or less. The vertical-velocity data were subjected to a high-pass filter that removed both INS biases and actual vertical-velocity variations with periods of 20 minutes or longer. The temperature data were taken from the RAF reverse-flow temperature sensor, which has an accuracy of 0.14 K. Flight-level data were measured at the rate of 5 Hz and averaged over periods of 1 s, producing independent observations at a frequency well within the observing capabilities of the relevant instruments.

The flight pattern of the aircraft consisted of passes at various levels oriented approximately normal to the surface frontal position. The data were adjusted to remove a systematic temperature trend and projected onto a moving x–z plane normal to and relative to the coastal front, in the manner described by NiNe, except that the entire domain moves with the front. Positive distance (and positive u component of the wind) is directed toward the warm side of the coastal front, and positive v indicates air moving parallel to the front with warm air to the right. Aircraft heights are estimated hydrostatically from flight-level air-pressure and independent surface-pressure observations.

Because no aircraft passes were flown parallel to the coastal front, the orientation of the observed waves cannot be directly determined from the observations. This is a serious limitation of the data. However, it will be shown from dynamical considerations in section 4 that the waves were oriented approximately parallel to the coastal front and normal to the aircraft track. Most of the diagnostic calculations will assume that the waves are oriented normal to the aircraft track.

For analysis of the wave characteristics, the data, which are equally spaced in time, will be assumed to be equally spaced in distance. Since the airspeed of the aircraft was held fairly constant on any given pass, the largest data-point spacing errors introduced by this assumption are only 2% to 3% and do not affect estimates of wavelength.

b. Theoretical framework

For assessing the stability characteristics of the observed flow, the two-dimensional equations of motion, the thermodynamic equation, and the mass continuity equation are linearized about a basic state characterized by a mean potential temperature θ_o and a horizontal wind U and Brunt–Väisälä frequency N that are functions of height alone. Flow is assumed to be inviscid, adiabatic, Boussinesq, and incompressible, and the effects of the earth's rotation are neglected. The perturbation variables are assumed to possess plane wave structures of the form

$$a = \mathrm{Re}\{\hat{a}(z)\exp[ik(x - ct)]\} \tag{1}$$

where a represents any of the four variables (u, w, θ, π), $\hat{a}(z)$ is the height-dependent complex amplitude, k is the wavenumber in the x direction, and $c = c_r + ic_i$ is the complex phase speed.

The equations governing the perturbation variables may be reduced (e.g., Miles 1961) to a single equation for the vertical structure of w, known as the Taylor–Goldstein equation:

$$\frac{\partial^2 \hat{w}}{\partial z^2} + \Lambda(z)\hat{w} = 0 \tag{2a}$$

where

$$\Lambda(z) = \frac{N^2}{(U-c)^2} - \frac{\partial^2 U/\partial z^2}{(U-c)} - k^2. \tag{2b}$$

Neutral modes ($c_i = 0$) are vertically propagating if the stratification and wavelength are large and the curvature of the wind profile and the local phase speed relative to the background flow are small. Unstable

modes ($c_i > 0$) are prohibited if the local Richardson number,

$$\mathrm{Ri} = N^2 \Big/ \left(\frac{\partial U}{\partial z}\right)^2,$$

is everywhere greater than 0.25 (Miles and Howard 1964).

Among the classes of instabilities governed by (2) are Kelvin–Helmholtz instabilities, Holmboe instabilities (Holmboe 1962), and resonant gravity wave instabilities (Davis and Peltier 1976; Rosenthal and Lindzen 1983). Of these, only the first two are relevant to the present situation, because the ambient stratification outside the coastal front inversion ($N^2 = 2 \times 10^{-4}$ s^{-2}) is much too weak to allow gravity wave propagation at the observed wavelengths (1500 m) and phase speeds ($U - c = -7$ m s^{-1}).

c. Polarization relations

The polarization relations associated with (1)–(2) may be written as

$$\hat{\theta} = \frac{\theta_0 N^2}{g}\hat{\eta} = \frac{i\theta_0 N^2 \hat{w}}{kg(U-c)} \tag{3a}$$

$$\hat{u} = \frac{i}{k}\frac{\partial \hat{w}}{\partial z} \tag{3b}$$

where η is the vertical parcel displacement. These equations specify the local phase relationships between u, w, η, and θ as a function of Λ and will be used to diagnose such quantities as the local wave amplitude $|\eta|$, the local phase speed, the height of the critical level, the growth rate, and the wave amplitude at the critical level from spectral analyses of u, w, and θ. Equation (3a) may be rewritten as

$$\hat{\theta} = \left[\frac{\theta_0 N^2 \hat{w}}{kg[c_i^2 + (U-c_r)^2]}\right][-c_i + i(U-c_r)] \tag{4}$$

which, given the local basic-state values of U and N, determines c_r and c_i as functions of the amplitude ratio and phase difference between w and θ and illustrates (DeBaas and Driekonks 1985) that the ratio of the real-to-imaginary phase speeds may be determined from the ratio of the (w, θ) cospectrum and quadrature spectrum. Application of a WKB approach to (3b) indicates that w and u should be 90° out of phase where the wave is evanescent and 0° or 180° out of phase where the wave is vertically propagating.

The actual phase relationships contained in the data may be detected through judicious application of cross-spectrum analysis. The means and linear trends are removed from all time series prior to spectral or cross-spectral analysis. Two-sided spectra are computed using Institute of Mathematics Subroutine Library (IMSL) subroutines, which are based on definitions given by Jenkins and Watts (1968). No smoothing is applied to the spectra in the cases (section 3) in which the time series nominally contain a small integral number of waves; otherwise a 7-point moving average is applied.

d. Method of solution of the instability eigenvalue problem

Equation (2), together with suitable boundary conditions, represents an eigenvalue problem for the complex phase speed c as a function of $U(z)$, $N(z)$, and k. Our method of solution is fourth-order Runge–Kutta numerical integration and is similar to the shooting methods employed by Lalas and Einaudi (1976) and Merrill (1977). Possible eigensolutions corresponding to imaginary phase speeds less than 0.01 m s^{-1} were ignored, as were phase speeds and growth rates prohibited by the semicircle theorem (Miles 1961; Howard 1961). Between 400 and 1200 vertical grid points were generally necessary for determination of c_r and c_i. The numerical algorithms were tested by comparing solutions with the results given in Hazel's (1972) Figs. 1 and 3 for symmetrical hyperbolic tangent profiles, and no differences were found.

The observed vertical structure of the lower atmosphere (presented in section 3) included a weakly stratified region between the ground and the coastal front inversion. Above the coastal front inversion, a second evanescent region extended upward to a strong warm frontal inversion at 1140 m above sea level. As suggested by this configuration, we solve (2) under the conditions of rigid boundaries at the ground and at the base of the warm frontal inversion. Growth rates and real phase speeds of the fastest-growing modes were found to differ by less than 1% if a realistic warm-front inversion was placed between 1100 and 1400 m, with upward wave propagation allowed above 1400 m.

3. Observations of large-amplitude waves

a. Flight track of the aircraft

The aircraft sampled the coastal front inversion and its environment in a series of quasi-horizontal passes separated vertically by 100 to 600 m, relevant portions of which are shown in Fig. 1. The approximate locations of frontal boundaries and inversions, as identified by bounding isotherms, are given for reference; more detailed analyses of the temperature and wind structure of this and other coastal front cases may be found in NiNe.

b. Directly observed basic-state vertical structure: Sounding 2

The flight track included three extended segments in which the aircraft ascended or descended at a rate of 4 m s^{-1} or greater, producing vertical profiles of atmospheric structure. The first such sounding occurred prior to pass 1, entirely within the warm air, and is not

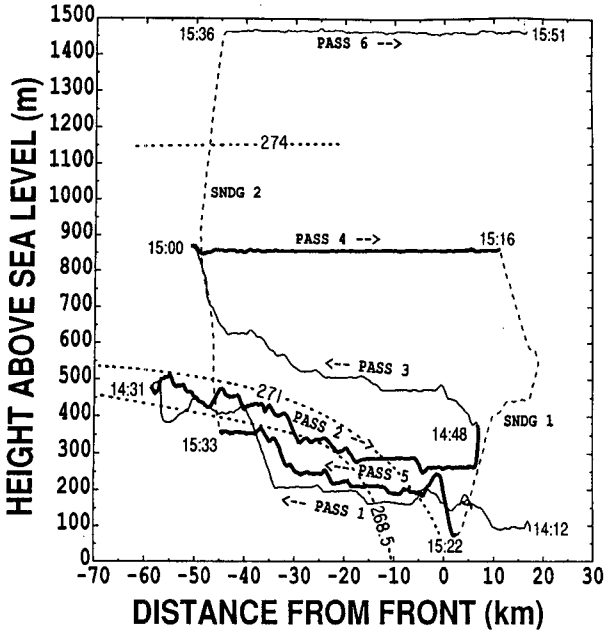

FIG. 1. Flight track of aircraft in vicinity of coastal front during 4 Dec 1983, projected onto a plane normal to the coastal front. Individual passes and soundings are labeled, and times at end points are given in UTC. Isotherms are drawn schematically to indicate the approximate locations of the coastal front inversion (between 268.5 and 271 K) and the warm-front inversion (above 274 K).

depicted in Fig. 1. The next sounding, designated sounding 1, also occurred within the warm air. The sounding of greater interest, sounding 2, began below the coastal front inversion and terminated within the warm-front inversion.

Figure 2 shows raw and smoothed profiles of potential temperature and horizontal wind components from sounding 2, along with local Richardson numbers (with respect to both u and the total wind) calculated from the smoothed profiles. The smoothing algorithm is described in section 4b. The base of the graph was chosen to approximately coincide with ground level. The typical glide slope during the ascent was 10%, and the apparently unstable stratifications found in the raw data in the lower sections are attributable to horizontal variations in temperature.

In Fig. 2 the base of the warm-frontal inversion is found in both the u and θ profiles at 1140 m. Air between this level and the top of the profile will be considered to be within the warm-front inversion. The top of the coastal front inversion, at 630 m, is also well defined in both u and θ. Air between the coastal front inversion and warm-front inversion will be referred to as warm air or marine air. The base of the coastal front is not distinct, and we choose to place it at 520 m, below which θ is nearly constant, u becomes highly variable, and v decreases in magnitude. Air beneath

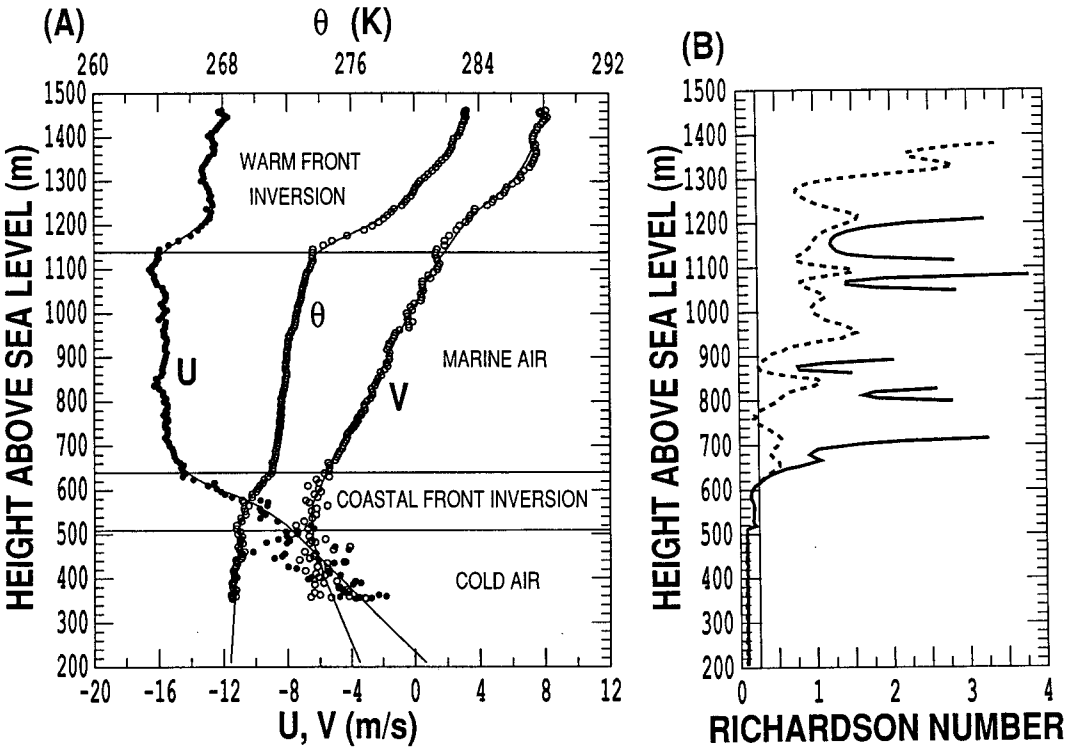

FIG. 2. (a) Vertical profiles of front-normal wind u (solid circles), front-parallel wind v (open circles), and potential temperature θ (open circles) observed by aircraft during sounding 2. The smoothed profiles used for the stability analysis in section 4b are given by the solid lines. The nominal vertical margins of the inversions are identified. (b) Vertical profiles of Richardson number obtained from the smoothed profiles in (a). The solid line is Ri calculated using the front-normal wind u, while the dashed line is Ri calculated from the full vector wind shear in each layer.

this inversion will be referred to as cold air. For any layer, the bulk Richardson number is computed using the total shear, stratification, and layer depth.

The cold-air layer beneath the coastal front inversion features the largest high-frequency excursions of wind and temperature, which show variations of approximate amplitude 1.6 m s^{-1} (u), 1.3 m s^{-1} (v), and 0.2 K (θ). Consistent with the large amount of observed turbulence is a low bulk Richardson number for the layer of 0.1. Turbulence is to be expected in the cold-air layer because the v component of the wind is antitriptic (Bell and Bosart 1988; NiNe), and Reynolds stresses are required throughout the cold air to balance the ambient along-mountain pressure gradient. The potential temperature appears to be nearly well mixed, but the large vertical gradient in the u component of the wind is unexpected.

Within the coastal front inversion, small-scale variations are still present, but the amplitudes of the wind oscillations have decreased by about a factor of 3. The v component of the wind has its largest negative value at the base of the inversion and is nearly constant within the inversion, while the u component exhibits strong shear. The bulk Richardson number for the inversion, being so close to 0.25, suggests the possibility that Kelvin–Helmholtz instability may be acting to maintain the Richardson number near a neutral value, opposing the tendency of larger-scale forces (for example, the mixing of u beneath the inversion) to reduce the Richardson number. Similar evidence for the maintenance of neutrality along frontal inversions was found by Browning et al. (1970).

Above the coastal front inversion, the marine-air layer is weakly stratified and possesses a typical Richardson number greater than 0.5, prohibiting deep shear instabilities. The flow toward the mountains is nearly uniform in the vertical, while the v component profile is remarkably close to a straight line. The marine-air layer is capped by a warm-front inversion that also exhibits a stable Richardson number.

Before proceeding with the description and analysis of the waves, we note that across the total depth of the coastal front inversion, the potential temperature changes by 2.3 K and the u component of wind by 6.7 m s^{-1}.

c. *The pass 2 wave train*

Figure 3 presents the θ and u records from the first four aircraft passes. To remove the smallest-scale variations, the data have been passed through a 5-point running mean filter, roughly equivalent to averaging over 0.4 km. Passes 3 and 4 remain in the marine air over the coastal front inversion, and their traces tend to be smooth. The separation of pass 3 and pass 4 temperature traces in the first 25 km indicates that weak stratification develops within the marine air as it passes over the coastal front inversion. The u wind speed also becomes increasingly negative with distance behind the front, showing the acceleration of the marine air over the dome of cold air.

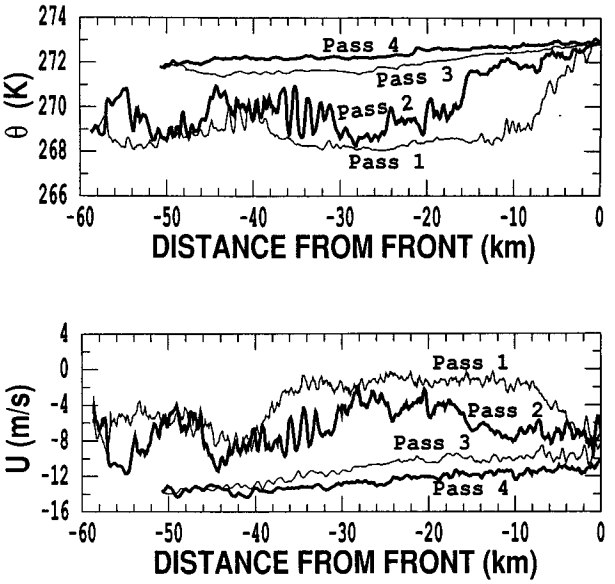

FIG. 3. Potential temperature θ and front-normal wind u observed by aircraft during passes 1 through 4, as a function of horizontal position. The data have been smoothed with a 5-point running mean filter.

Passes 1 and 2 penetrated beneath the coastal front inversion. The aircraft remained below the inversion for most of pass 1, and a comparison of wind and temperature from passes 1 and 3 between −8 and −35 km provides a good measure of the magnitude of the air mass difference across the coastal front inversion. The data from pass 2 lie between passes 1 and 3 and show large variations that are sometimes related to variations in aircraft height, indicating that the aircraft was in the neighborhood of the coastal front inversion during most of pass 2.

The waves that first drew attention to this case were found between −32 and −37 km during pass 2. From Fig. 3 it may be seen that the total span of the variation in θ during the oscillations is comparable to the total difference between the cold air (pass 1) and the marine air (pass 3). The variations in u do not quite span that range, but are still large compared to other variations observed during the flight.

The unsmoothed 1-s data record in the vicinity of the waves is shown in Fig. 4. The θ and u variations are clearly 180° out of phase. The amplitudes and phase difference, combined with the sudden transitions between peaks and troughs, suggest that the variations are due to vertical displacements of the coastal front inversion. Consistent with this picture are the variations in v and w, which like u are turbulent during the cold half of the wave and smoother during the warm half of the wave. Recall from section 3b that air beneath the inversion was much more turbulent than air above the inversion.

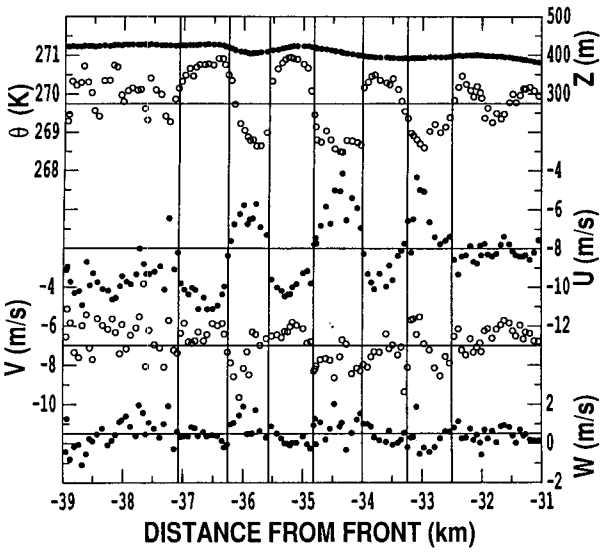

FIG. 4. Unfiltered 1-s flight-level data from pass 2, showing horizontal wave structure. Vertical lines are drawn at approximate half-wavelength intervals; horizontal lines are added as an aid in discerning the values of individual data points. From top to bottom, the graphs are of the height z of the aircraft (solid circles), potential temperature θ (open circles), front-normal wind speed u (solid circles), front-parallel wind speed v (open circles), and vertical wind speed w (solid circles).

Further information on the amplitudes and phases of the variations are obtained from a raw spectral analysis of the section from −32.5 to −37.1 km. Aspects of the wavenumber 3 component of the spectra are given in Table 1. The data for the Fourier decomposition of the altitude of the aircraft are included to confirm that the observed waves were not artifacts of changes in altitude, and indeed the phase relationship suggests that the altitude variations were caused by the headwind variations.

The large oscillations of u and θ dominate their respective variances. An oscillation of v is found that is in phase with θ, but the magnitude of the oscillation is weak compared to oscillations at other periods; three other wavenumbers have a larger fraction of the variance. The lack of a dominant signal in v is evidence that, if the waves are being generated by shear within the inversion, the shear and wavenumber vectors are oriented nearly parallel to the flight track of the aircraft and normal to the coastal front. The w wavenumber 3 oscillation has the largest fraction of the w variance, even though the amplitude is weak.

The w oscillation is mostly in phase with u and out of phase with θ, implying from (4) and (3b) that the observations are taken near the steering level. The ratio of the Doppler-shifted phase speed to the growth rate may be estimated from the cospectrum $C_{w\theta}$ and quadrature spectrum $Q_{w\theta}$, which from (4) yields

$$\frac{(U - c_r)}{c_i} = \frac{-Q_{w\theta}}{C_{w\theta}} = -0.39, \qquad (5)$$

indicating that (since the phase shows that the waves are amplifying) the aircraft is perhaps slightly above the critical level. We may further estimate the magnitudes of the real and imaginary phase speeds using (4). The results of such a calculation must be viewed with caution, since the waves, while not yet breaking, appear to be well beyond the linear regime; vertical displacements appear to be comparable to the depth of the inversion. However, we may at least obtain a rough estimate of the growth rate.

To solve (4), we estimate $U = -8$ m s^{-1}. Assuming $c_r \approx U$, the wavenumber k is estimated to be 3.65×10^{-3} m^{-1} (wavelength 1720 m). By far the largest uncertainty lies in the estimate of the vertical gradient of potential temperature, since the stratification may vary considerably over one wavelength because of the apparently high amplitude of the oscillation. Using the mean stratification within the inversion from Fig. 2, we take $\Delta\theta/\Delta z = 2°/150$ m. With these numbers, we obtain $c_i = 0.77$ m s^{-1} and $c_r = -7.7$ m s^{-1}. Because of the lack of synchronous observations of N and the lack of consistency of w from wave to wave (Fig. 4), the actual c_i may possibly lie anywhere from 0.4 to 3.0 m s^{-1}, which implies a growth rate between 1.46×10^{-3} s^{-1} and 10.95×10^{-3} s^{-1}. With this range, (3b) yields a range of vertical displacement amplitudes of $23 \text{ m} \leqslant |\eta| \leqslant 137$ m.

TABLE 1. Raw spectral characteristics of pass 2 waves (depicted in Fig. 4) from time series of aircraft data between −37.1 and −32.5 km containing three complete wavelengths. Total number of data points $N = 70$.

	(a) Wavenumber 3 spectral analysis			(b) Wavenumber 3 cross-spectral analysis				
		Fraction of total variance explained			Cospectrum	Quadrature spectrum	Cross-amplitude	Phase (deg)
	Amplitude	Percent	Rank	x, y	$2C_{xy}/N$	$2Q_{xy}/N$	$2\alpha_{xy}/N$	ϕ_{xy}
u	1.89 m s^{-1}	72.5	1	u, v	−0.79 m^2 s^{-2}	0.03 m^2 s^{-2}	0.79 m^2 s^{-2}	−178
v	0.42 m s^{-1}	12.6	4	u, θ	−1.73 K m s^{-1}	0.17 K m s^{-1}	1.74 K m s^{-1}	−175
w	0.25 m s^{-1}	11.7	1	u, z	−4.16 m^2 s^{-1}	4.29 m^2 s^{-1}	5.98 m^2 s^{-1}	−134
θ	0.92 K	72.7	1	w, u	0.42 m^2 s^{-2}	0.21 m^2 s^{-2}	0.47 m^2 s^{-2}	−27
z	3.17 m	13.8	2	w, θ	−0.21 K m s^{-1}	−0.08 K m s^{-1}	0.23 K m s^{-1}	159

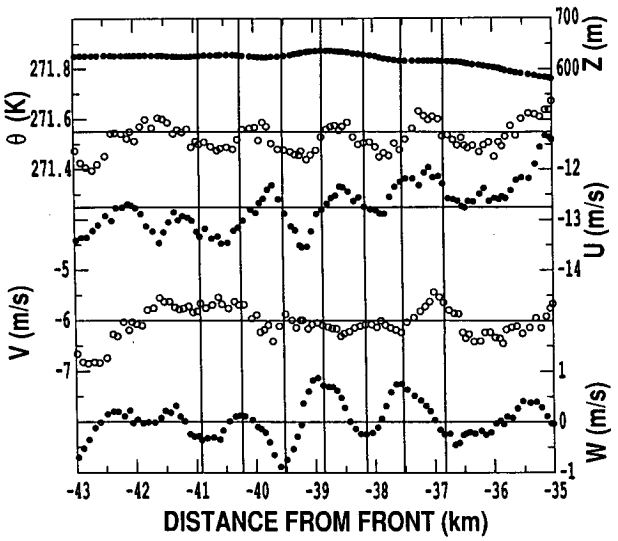

FIG. 5. Unfiltered 1-s flight-level data from pass 3, showing horizontal wave structure. Plots are as in Fig. 4, except that the vertical scales have been expanded.

d. *The pass 3 wave train*

Inspection of the data from pass 1 (Fig. 3) does not indicate the presence of coupled oscillations later observed during pass 2. Some oscillations are indeed found, particularly in the wind, but there is no local maximum in wave activity near −29 km, where the waves would have been during pass 1 if the estimated c_r from section 3c is accurate. The waves near −34 km are both too far west and too short to be the waves later observed in pass 2.

By the time of pass 3, the pass 2 waves would have been located near −45 km. Inspection of that section of the time series reveals smooth, generally coherent variations in u and w with wavelengths between 1.1 and 1.8 km, but no set of three regularly spaced waves of the wavelength observed in pass 2. The plane was ascending during that segment of pass 3, and the temperature data show little coherence with the wind data.

Prior to the beginning of the ascent, regular waves were observed in pass 3 between −37 and −41 km in both the temperature and wind (Fig. 3). The complete set of relevant parameters from that segment of pass 3 are shown in Fig. 5. It is immediately apparent that there is much less short-wavelength variation in the wind components compared to Fig. 4, even though the vertical scales in Fig. 5 have been expanded. Furthermore, the amplitudes and phases are quite different (Table 2).

The strongest signals are present in u, w, and θ. The phase difference between w and θ is 91.5°, implying from (4) and (5) that $(U - c_r)$ is negative and much larger than c_i. Because the phase shift is so close to 90°, we will not attempt to estimate c_i, but c_r may be approximately determined. To determine the Doppler-corrected wavelength, we assume $c_r \approx -7$ m s^{-1}, which yields a wavelength of 1.26 km. Here U is determined to be −12.7 m s^{-1}, and the vertical gradient of θ is estimated from Fig. 2 to be 1 K/300 m. Using (4) and assuming $|U - c_r| \gg |c_i|$, we obtain $c_r = -6.8$ m s^{-1}, which is in fair agreement with the estimate obtained for the pass 2 waves. Although linearity should be a reasonable assumption for the observed waves at this height, there is still uncertainty introduced by the estimate of N. The actual local value of $\Delta\theta/\Delta z$ could conceivably differ by 50% from our estimate, implying a possible range of phase speeds of -9.7 m s$^{-1} \leqslant c_r \leqslant -3.9$ m s^{-1}. From (3a), this implies a local amplitude range of 8 m $\leqslant |\eta| \leqslant$ 25 m.

The phase difference of 95° between w and u implies that the wave is vertically evanescent and is decaying upward. As a first attempt at application of (3b), we assume that we are in an evanescent region of constant U and N bounded above by a rigid lid (the warm front). Equation (2) then admits solutions of the form

$$\hat{w} = A \sinh\{|\Lambda|^{1/2}(z - z_{lid})\} \tag{6}$$

that, when combined with (3b), yields

$$\hat{u} = \frac{i|\Lambda|^{1/2}}{k}\hat{w}\coth\{|\Lambda|^{1/2}(z - z_{lid})\} \approx \frac{i\hat{w}}{k(z - z_{lid})} \tag{7}$$

the latter approximation following if Λ is small.

TABLE 2. Raw spectral characteristics of pass 3 waves (depicted in Fig. 5) from time series of aircraft data between −40.9 and −36.8 km containing three complete wavelengths. Total number of data points N = 48.

	(a) Wavenumber 3 spectral analysis			(b) Wavenumber 3 cross-spectral analysis				
		Fraction of total variance explained			Cospectrum	Quadrature spectrum	Cross-amplitude	Phase (deg)
	Amplitude	Percent	Rank	x, y	$2C_{xy}/N$	$2Q_{xy}/N$	$2\alpha_{xy}/N$	ϕ_{xy}
u	0.36 m s^{-1}	71.3	1	u, v	−0.017 m^2 s^{-2}	−0.014 m^2 s^{-2}	0.022 m^2 s^{-2}	139
v	0.06 m s^{-1}	3.4	5	u, θ	0.020 K m s^{-1}	0.001 K m s^{-1}	0.020 K m s^{-1}	−3
w	0.49 m s^{-1}	74.0	1	u, z	−0.248 m^2 s^{-1}	0.072 m^2 s^{-1}	0.259 m^2 s^{-1}	−164
θ	0.05 K	63.5	1	w, u	−0.016 m^2 s^{-2}	−0.179 m^2 s^{-2}	0.179 m^2 s^{-2}	95
z	0.71 m	0.8	3	w, θ	−0.001 K m s^{-1}	−0.027 K m s^{-1}	0.027 K m s^{-1}	92

From the values of U, N, and c_r listed above, we find that the first term in Λ [see Eq. (2b)] is 3.6×10^{-6} m^{-2} and the third term is -2.5×10^{-5} m^{-2}, so that $|\Lambda|^{1/2} \approx 0.9k$. Equation (7) then directly implies that $|u| \geq 0.9|w|$, which contradicts the observed value (Table 2) of $|u| = 0.73|w|$. This inconsistency arises because we have neglected the second derivative of the horizontal wind. The actual local value of $\partial^2 U/\partial z^2$ is impossible to accurately determine. From inspection of the region just above the inversion in Fig. 2, a rough estimate of $\partial^2 U/\partial z^2$ might be 1.5 m s^{-1}/(100 m)^2. Applying this number to (2b), we find that the second term in Λ is 2.5×10^{-5} m^{-2}, which is sufficient to make Λ positive! Since we know from the phase shift between w and u that Λ is negative, we now have a possible range of Λ of between 0 and $-0.9k$. To verify that this range is consistent with the ratio of u to w, we take the limit $\Lambda \to 0$ and use (7) to obtain $|u| \geq 0.43|w|$, which is indeed consistent with the observed ratio.

e. *Summary of observed wave characteristics*

The wave characteristics calculated in the previous sections are summarized in Table 3. From the calculated phase speeds, both sets of waves had steering levels within the coastal front inversion, implying Kelvin–Helmholtz or Holmboe instability as a likely generation mechanism. Kelvin–Helmholtz instability would be more consistent with the large vertical excursions of the entire frontal inversion inferred from the pass 2 time series. The observed wavelengths also appear to be consistent with the Kelvin–Helmholtz instability mechanism. Using the rule of thumb (e.g., Miles and Howard 1964) that the most unstable wavelength is 7.5 times the inversion depth gives an inversion depth of 200 m, which is larger than was observed locally during sounding 2, but is still consistent with the analyses presented in NiNe. We shall examine the unstable modes of the observed frontal inversion in a more rigorous fashion in section 4.

The local vertical displacement magnitude estimate for the pass 3 waves was much smaller than that for the pass 2 waves. This does not necessarily imply that the pass 2 waves had grown to larger amplitude than the pass 3 waves. A measure of the amplitude of linear Kelvin–Helmholtz waves is, using (3a),

$$k|\hat{\eta}|_{\max} = \frac{|\hat{w}|_{U=c_r}}{c_i}, \tag{8}$$

which is proportional to the aspect ratio of the waves. For pass 2, since w was measured near the steering level, (8) gives 0.32. For pass 3, we know neither w nor c_i. Anticipating the vertical structure calculations of the following section (see Fig. 7), we may postulate that the amplitude of w measured at flight level is within about a factor of 2 of the amplitude of w at the steering level. If the imaginary phase speeds of pass 2 and pass 3 waves were similar, (8) gives a pass 3 wave amplitude similar to that obtained for pass 2. The differences in the local amplitudes of the flight-level variables are largely attributable to the difference between the flight levels of pass 2 and pass 3 and the vertical structure of Kelvin–Helmholtz waves.

The growth rate estimate from pass 2 implies an e-folding time of a few minutes. If the pass 3 waves had a similar time scale of development, the waves should still have been present along the inversion five minutes later, when the aircraft made pass 4 at a height of 850 m (Fig. 1). Because pass 4 was relatively high above the inversion, the signature of the waves should have been much weaker than at pass 3. The search for waves in pass 4 is further complicated by the uncertainty in the phase velocity of the waves. Despite bandpass filtering and Doppler correcting for a range of possible phase speeds, the weak variations in the pass 4 data could not be made to fit the oscillations in the pass 3 data. The closest match was at $c_r = -7.9$ m s^{-1}, for which the filtered pass 4 u series matched the wave peaks at -37.2 and -41.3 km in pass 3, with a single peak (instead of two peaks) in between.

4. Linear instability analysis

a. *Introduction*

Several factors indicate that the waves should have begun their life cycles as quasi-linear unstable normal modes. The waves appear to be vertically confined to

TABLE 3. Characteristics of the pass 2 and pass 3 wave trains.

Parameter	Pass 2		Pass 3	
	Calculated value	Possible range	Calculated value	Possible range
Raw wavelength (m)	1535	1500 to 1570	1370	1340 to 1400
Phase speed (m s^{-1})	−7.7	−7.2 to −8.2?	−6.8	−3.9 to −9.7
Doppler-corrected wavelength (m)	1720	1680 to 1760	1260	1210 to 1300
Imaginary phase speed (m s^{-1})	0.77	0.4 to 3.0	Not estimated	Large
Growth rate (10^{-3} s^{-1})	2.8	1.4 to 11.0	Not estimated	Large
Amplitude of vertical displacements (m)	90	20 to 150	17	8 to 25

the neighborhood of the coastal front inversion. From the variation of u and v above the inversion, the waves are oriented roughly parallel to the coastal front. External forcing, from the surface topography, cannot have produced the observed waves because the wavelength is too short for the observed topography and the waves would have been oriented across the direction of the (northeasterly) surface wind. The waves cannot have propagated long distances along the inversion because, given the large shear present, severe distortions caused by the shear would develop on a time scale of less than five minutes. Finally, spectral analyses (section 5a) indicate that little energy is present at lower or higher harmonics of the observed waves, suggesting that there was little wave growth at other than the observed 1–2-km wavelengths.

No vertical profiles of temperature and wind were taken near the time of the observations of the high-amplitude waves. The most complete profile, from sounding 2 (Fig. 2), was taken 40 minutes after the pass 3 waves were observed and 1 hour after the pass 2 waves. Between the end of pass 3 and sounding 2, the most notable change in the local environment was an increase of 2.5 m s^{-1} in the magnitude of the wind component away from the front, part of which may be due to a slow inertial navigation system drift that can introduce errors of 0.5 m s^{-1} per hour of flight time. The temperature difference across the inversion appears to have changed little.

The simplest assumption to make would be that, after allowing for a bias in the wind speed, sounding 2 represents the basic state on which pass 2 and pass 3 waves developed. This assumption is shown in section 4b to be inconsistent with the hypothesis that the waves were produced by a linear instability mechanism. Two alternative assumptions would be that the basic state in sounding 2 has already been adjusted toward stability by waves such as those observed, or that the basic state varies in space and time between marginally stable and marginally unstable conditions. The latter assumption is supported by the lack of waves along other portions of the inversion or along other observed coastal front inversions (section 6). Further evidence for the latter assumption is the apparently narrow depth of the sounding 2 inversion, whereas Kelvin–Helmholtz instability should act to increase the thickness of the inversion (Thorpe 1973). Among the processes, other than shear instability that may have produced a stabilized profile, are included increased shear beneath the inversion, or destruction of the inversion from be- from increased turbulence. Thus, in section 4c, we consider a range of possible basic states possessing the same general structure as sounding 2 and estimate the sensitivity of the most unstable waves to such aspects of the basic state as the inversion thickness and the shear beneath the inversion. In section 4d we attempt to estimate from the available horizontal aircraft passes the values of the parameters found to most strongly determine the structure of the unstable waves.

b. Solutions using the sounding 2 vertical structure

To reduce sounding 2 to a form suitable for stability analysis, it is necessary to smooth the profiles and extend them down to the lower boundary. The smoothing was done by means of moving averages; the u and θ profiles were passed successively through 5-point, 7-point, and 3-point moving averages. To smooth the v profile, a 21-point moving average was substituted for the 7-point moving average in order to remove small-scale changes in sign of the vertical second derivative. Extrapolation to the ground was done with linear profiles. These profiles were chosen subjectively and joined to the smoothed profiles at a sufficient height (520 m for u and θ, 400 m for v) to eliminate the waviness beneath the inversion that remained in the smoothed profiles. The final smoothed and extrapolated profiles used in the stability analysis were presented in Fig. 2, along with Richardson numbers calculated from the final profiles.

A search for unstable waves using (2) failed to find unstable modes with wavelengths between 300 and 3000 m and steering levels near the inversion. The lack of unstable modes may imply that sounding 2 represents conditions during the decay stage of instabilities, or that the basic state has become marginally stable due to other processes. If so, a small increase in shear or decrease in stratification or inversion depth should be sufficient to make the profile unstable. We elect to test this hypothesis by decreasing the stratification.

Analyses are performed on profiles consisting of the observed winds, but with the observed N^2 multiplied by a constant factor ϵ that lies between 0 and 1. For unstable profiles this yields a single unstable mode whose steering level is near the center of the inversion. As ϵ is increased, the growth rate of the most unstable mode decreases linearly, while the most unstable wavelength remains nearly constant. Stability to infinitesimal modes is attained near $\epsilon = 0.85$, indicating that the sounding 2 profile is only weakly stable in this sense.

We now wish to examine the characteristics of these unstable waves to determine if they are similar to the observed waves. The growth rates and phase speeds as a function of wavelength and ϵ are shown in Fig. 6, and the vertical structure for the most unstable wavelength at $\epsilon = 0.5$ is shown in Fig. 7. The vertical structure and steering level are consistent with the observed waves and confirm our supposition in section 3 that Kelvin–Helmholtz modes (Rayleigh modes when $\epsilon = 0$) are the dominant instability characteristic of the basic flow.

The most unstable waves have a wavelength near 700–750 m, which is about a factor of 2 less than was observed. Wavelengths such as those observed are also unstable for those ϵ supporting instability, and the longer wavelengths should tend to grow to larger amplitude (Patnaik et al. 1976), but little energy was found in the observed fields at the smaller wavelengths. This

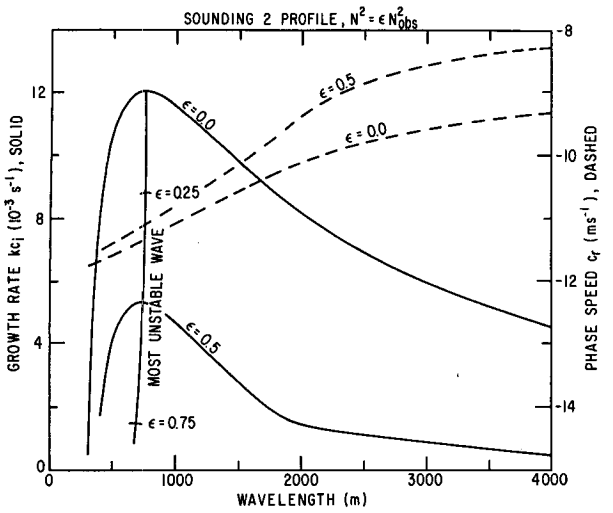

FIG. 6. Growth rate (solid) and phase speed (dashed) as a function of wavelength and ϵ for instabilities on the sounding 2 profile of u and θ, where the observed stratification has been reduced by the factor ϵ.

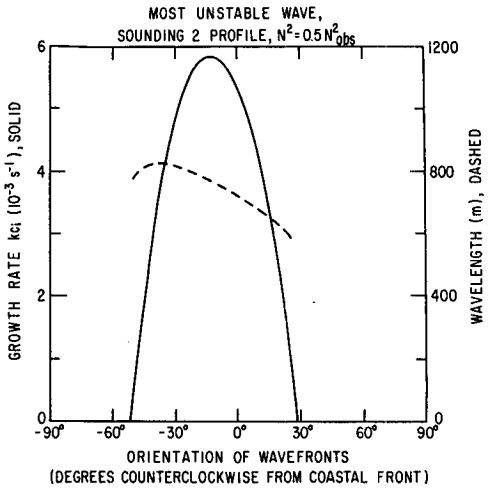

FIG. 8. Growth rate (solid) and wavelength (dashed) of the most unstable wave as a function of wave orientation, for the sounding 2 profile with stratification reduced by a factor $\epsilon = 0.5$.

discrepancy between the observed waves and the stability characteristics of the vertical basic state observed an hour later is the primary motivation for examining in section 4c the sensitivity of the unstable wave characteristics to changes in the basic state.

To determine whether the assumption that the waves are oriented normal to the coastal front is a reasonable one, we perform stability analyses for a range of orientations of wave fronts. We used the observed sounding 2 winds and chose $\epsilon = 0.5$. As seen in Fig. 8, the largest growth rates are found for waves rotated 10–15 degrees clockwise with respect to the coastal front. The vertical structure of the mode (not shown) is quite similar to the mode shown in Fig. 7. In Fig. 2 it may be seen that a slight amount of positive shear is present in the v component across the inversion, so the most unstable wave orientation is consistent with the waves being normal to the shear vector within the inversion. We conclude that if the sounding 2 wind structure is representative of conditions that produced the observed waves, the waves were most likely oriented at an angle of 10–15 degrees relative to the airplane track. Such an angle would produce an error of less than 5% in the observed wavelength, and the changes implied for the calculations in section 3 would remain small compared to previously stated sources of error.

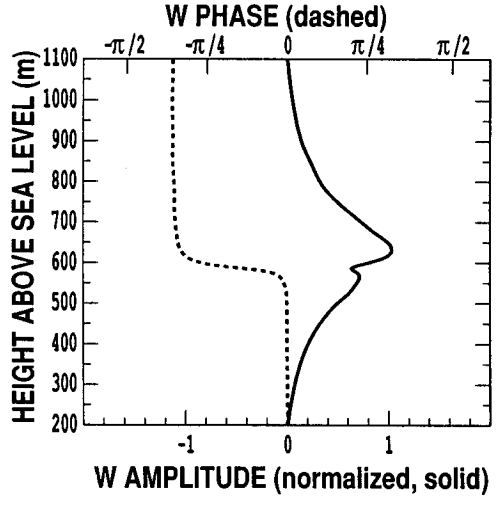

FIG. 7. Vertical structure of the most unstable mode for the sounding 2 profile with stratification reduced by a factor $\epsilon = 0.5$.

c. *Stability analyses of fully specified profiles*

For an analytic model that represents the essential features of the sounding 2 profile, we represent the frontal inversion as a hyperbolic tangent function of wind speed and potential temperature and represent the air masses above and below the inversion with linear profiles of wind speed and potential temperature. The basic features of this representation are shown in Fig. 9. This profile form is designed to prohibit singularities in Λ and to only allow instabilities based at or near the inversion level. A profile of y (where y may be either potential temperature or wind speed) is completely specified by the height of the upper and lower boundaries (z_t and z_b), the values of y at the upper and lower boundaries (y_t and y_b), the values of $\partial y/\partial z$ at the upper and lower boundaries (m_{yt} and m_{yb}), the height and half-width of the inversion (z_{iy} and δ_y), the half-magnitude of the change in y across the inversion (y_δ), the value of y at the midpoint of the inversion (y_i), and the height of the transition levels z_{liy} and z_{uiy} between the linear profiles and the hyperbolic tangent profiles.

The profile is overdetermined by the specification of four matching conditions, namely, that both y and

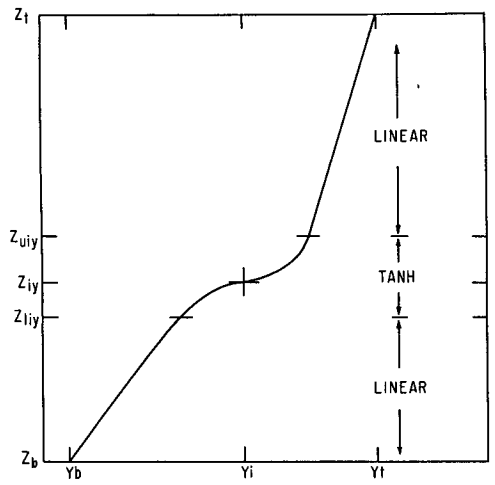

FIG. 9. Schematic diagram illustrating the specification of the vertical structure of an arbitrary parameter y (wind speed or potential temperature) as a linear function of z in the upper and lower layers and as a hyperbolic tangent profile in the middle layer, with continuous first derivatives at the layer boundaries.

dy/dz be continuous at z_{liy} and z_{uiy}, as drawn in Fig. 9. We shall allow these matching conditions to determine y_i, y_δ, z_{liy}, and z_{uiy} as implicit functions of the remaining eight parameters.

The parameter values chosen for the control profiles, intended to be representative of preinstability conditions near −35 km, are listed in Table 4. Most of the parameters are chosen by adjusting the basic structure of sounding 2 toward typical single-level values observed during passes 1, 2, 3, and 4. The control profile half-widths δ_θ and δ_u, while realistic, are purposely chosen to produce Kelvin–Helmholtz instability at a wavelength close to that of the observed waves. The parameters that are least well known and may strongly affect the instability dynamics are the depth of the inversion and shear layer (δ_θ and δ_u) and the wind profile beneath the inversion (u_b and m_{ub}).

The growth rates and phase speeds for the unstable modes of the control profile is shown in Fig. 10. The patterns are similar to those found for the reduced-stratification sounding 2 profile (Fig. 6), although the most unstable wavelength has shifted to 1075 m. (Unless otherwise stated, only a single branch of instability, identified as the Kelvin–Helmholtz branch, is found for the profiles considered.) The vertical structure of

TABLE 4. Parameter values used for control profile (see text and Fig. 9).

z_b	200 m	z_t	1100 m
u_b	0 m s^{-1}	θ_b	268 K
m_{ub}	−0.015 s^{-1}	$m_{\theta b}$	0.0033 K m^{-1}
u_t	−14 m s^{-1}	θ_t	272.5 K
m_{ut}	−0.001 s^{-1}	$m_{\theta t}$	0.0025 K m^{-1}
z_{iu}	500 m	$z_{i\theta}$	500 m
δ_u	75 m	δ_θ	75 m

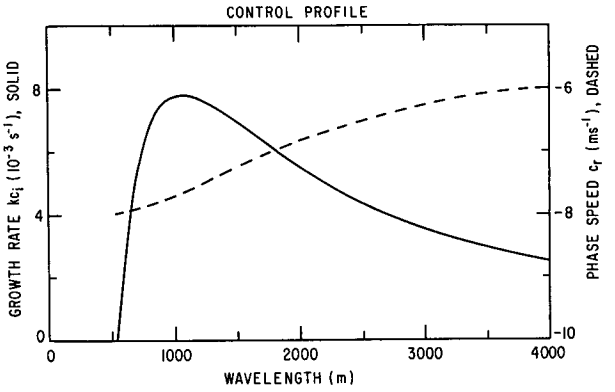

FIG. 10. Growth rate (solid) and phase speed (dashed) as a function of wavelength for instabilities on the control profile, defined in the text, Fig. 9, and Table 4. Compare with Fig. 6.

the most unstable mode (not shown) is similar to the most unstable mode for the modified sounding 2 profile (Fig. 7). The wavelength of the short-wave cutoff (550 m) is also larger than for sounding 2. As in sounding 2, no long-wave cutoff is found, in agreement with Hazel's (1972) results for hyperbolic tangent profiles that the proximity of the lower and upper boundaries causes the long waves to be destabilized. The real phase speeds of the waves are consistent with the observed phase speeds, as are the growth rates.

As has been found in previous studies of Kelvin–Helmholtz instability, the most unstable wavelength is a nearly linear function of the depth of the shear zone/inversion (Fig. 11). As seen in Fig. 11, the basic vertical structure of the frontal inversion may potentially support most unstable waves with wavelengths arbitrarily small or as large as 2.5 km. Further discussion regarding determination of the actual inversion depth is contained in section 4d.

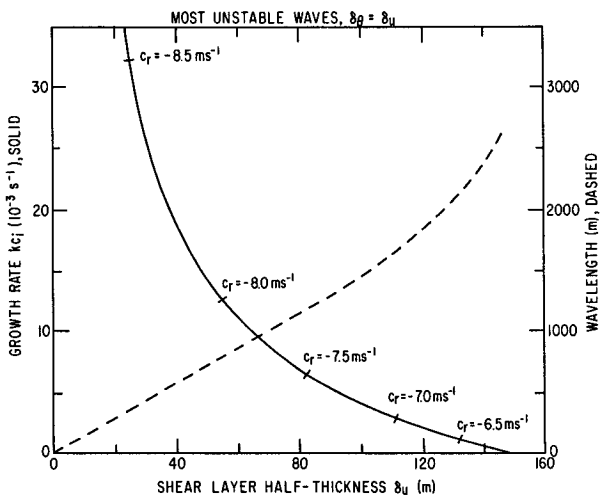

FIG. 11. Growth rate (solid), wavelength (dashed), and phase speed (marked along growth rate curve) of the most unstable wave as a function of shear-/inversion-layer thickness, with other parameters as in the control profile.

The growth rate is zero in Fig. 11 for $\delta_\theta = \delta_u \geq 150$ m. At smaller thicknesses, the maximum growth rate steadily increases, while the phase speed decreases. While part of the change in phase speed with inversion thickness is due to the destabilization of shorter wavelengths, modes at fixed wavelength (not shown) also experience a change in phase speed.

Calculations were also performed varying the shear beneath the inversion and the proximity of the lower boundary. Little sensitivity was found to either parameter within realistic ranges.

In contrast, if the depths of the shear and inversion layers are varied independently, the growth rate, phase speed, and wavelength of the most unstable wave change considerably. These values are shown as a function of δ_u and δ_θ in Fig. 12. Below the line $\delta_u = \delta_\theta$, which was examined in Fig. 11, the most unstable wave depends most strongly on the depth of the shear layer. As the shear-layer depth increases, the wavelength increases, the phase speed decreases, and the growth rate rapidly decreases. Quite different behavior is found for $\delta_u \gg \delta_\theta$. In that regime, the wave takes the form of Holmboe instability (Smyth and Peltier 1989), and a second Holmboe mode (not shown) is present above the inversion, with a phase speed between -9 and -13 m s^{-1}. Between the two regimes, the Kelvin–Helmholtz mode smoothly merges into the lower Holmboe mode, with small changes in the shear or inversion depths introducing comparatively large changes in wavelength, phase speed, and wavelength.

Perhaps the most striking feature of Fig. 12 is how rapidly the most unstable wavelength changes with small changes in the shear-layer thickness for parameter values close to those observed in sounding 2. For an inversion half-thickness of 50 m, an increase in the shear-layer half-thickness from 76 to 86 m is sufficient to increase the most unstable wavelength from 1260 (corresponding to pass 3) to 1720 m (corresponding to pass 2).

d. Estimation of actual basic-state inversion structure

It is clear that the structure of the unstable modes depends strongly on details of the thickness of the frontal inversion. We now attempt to estimate this thickness from the aircraft observations, although because the most unstable wave is so precisely specified by the inversion and shear thicknesses, the best estimates of the actual thicknesses may be those obtained from the linear instability analyses.

An observational estimate of the pre-instability inversion thickness may be made from pass 2. The rapid transitions between warm and cold temperatures are in effect cross sections through the sloping inversions, and if the geometrical shape of the inversion were known, the initial thickness could be determined.

A basic asymmetry was present in the transitions between warm and cold temperatures. As the aircraft traveled toward the coastal front (from left to right in Fig. 4), temperatures tended to rise abruptly and fall comparatively gradually. This structure is consistent with the well-known nonlinear evolution of Kelvin–Helmholtz billows (for example, see Klaassen and Peltier 1985). The sharp temperature rises in Fig. 4 would correspond to thin sheets of concentrated temperature

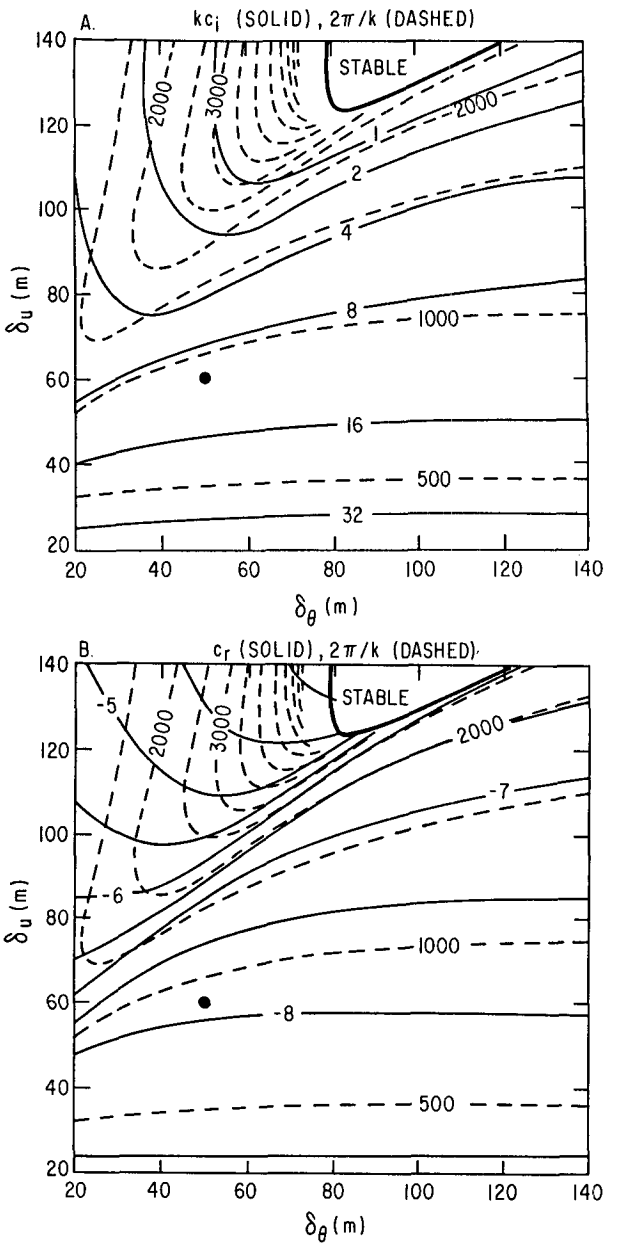

FIG. 12. (a) Growth rate (solid, 10^{-3} s^{-1}) and wavelength (dashed, m), and (b) phase speed (solid, m s^{-1}) and wavelength (dashed, m) of most unstable waves, as a function of the inversion- and shear-layer thicknesses. The unstable mode plotted corresponds to the Kelvin–Helmholtz mode and the Holmboe mode, whose steering level is located beneath the inversion. A second Holmboe mode (not shown) is present for large shear-layer thicknesses and small inversion thicknesses. The dot represents the approximate location in parameter space of the smoothed sounding 2 profile.

gradient, known as braids, while the gradual falls would correspond to the vortex roll-up region.

The numerical simulations of Klaassen and Peltier and others show that closed elliptical streamlines characterize the vortex roll-up region. If we assume that the shape of the streamlines stays roughly constant (a poor assumption, but we have little choice), the minimum horizontal length of transition between warm and cold temperatures in the vortex roll-up region just prior to overturning is given by the major axis of the closed streamline that is tangent to the bounding isotherms of the inversion. Approximating the aspect ratio of the tangent closed streamline by the aspect ratio of the largest closed streamline, the following relation is obtained:

$$\frac{|\eta|}{2\lambda} = \frac{\delta_\theta}{\Delta x_{\text{obs}}} \tag{9}$$

where $|\eta|$ is the maximum parcel displacement amplitude of the wave, λ is the wavelength, δ_θ is the half-thickness of the inversion, and Δx_{obs} is the horizontal distance over which the observed transition in temperature occurs. Taking the total temperature difference across the inversion to be 3.2 K, the half-thickness corresponds to a temperature difference of 1.6 K. From Fig. 4, a temperature drop of this size occurred over an average period of 5 s, compared to the total transit time across an individual wavelength of 23 s. Substituting into (9), this gives

$$\delta = 0.43|\eta|. \tag{10}$$

For the section 3c amplitude range estimate of 23 to 137 m, the possible range of inversion half-thicknesses is 10 to 59 m. The lower end of this range corresponds to Holmboe instabilities for which the observed wavelength is not the most unstable wave. The upper end (35 to 59 m) is consistent with both the instability analysis and the observed sounding 2 inversion thickness.

A final consistency check may now be made using (3a). Taking $\delta = 50$ m, the predicted growth rate from the instability analysis is 2.95×10^{-3} s^{-1}. From (10), the expected value of $|\eta|$ is 116 m. Equation (3a) then yields $|w| = 0.34$ m s^{-1}, which is consistent with the observed value from Table 1 of 0.25 m s^{-1}.

5. Evidence for breaking Kelvin–Helmholtz billows

a. Pass 3 cross-spectral analysis

The large-amplitude wave phase of Kelvin–Helmholtz instability occurs for only a short period in its life cycle prior to wave breaking. The presence of a few large-amplitude waves in the 4 December 1983 coastal front inversion implies that overturning Kelvin–Helmholtz billows should also be present. Within the breaking billows, aircraft time series of temperature and wind would exhibit strong high-frequency variations, while above the billows, the flow would tend to remain smoothly periodic. Visual examination of the wind record from pass 3 (Fig. 3b) indicates an apparently continuous series of smooth, wavelike oscillations between −25 and −50 km, implying the presence of billows in the inversion underneath. The 1-s unsmoothed data (not shown) also clearly show the oscillations, while high-frequency turbulence appears to be confined to the range 0 to −25 km. The turbulence appears to increase toward 0 km, attaining an amplitude characteristic of time series from the warm side of the coastal front.

To quantify the variations in both the waves and the turbulence, the pass 3 time series is split in two at −25 km, and a cross-spectral analysis is performed on the adjoining sets of 330 data points separately. For comparison, a cross-spectral analysis is also performed on a comparable period of data from 400 m as the aircraft was approaching the coastal front from offshore for the first time, a little more than one hour prior to pass 3. Selected results from the analysis are shown in Fig. 13. The desired waves appear as prominent peaks in the power spectra of u and w between 1 and 2 km, with a lesser peak present in θ at the same wavelengths. The wavelike nature of the peaks are confirmed by the coherence and phase spectra, which indicate a typical coherence of 0.85 between w and u and a phase shift of 85°. The coherence is less between w and θ, but the phase shift is again near 90°, as expected for evanescent waves generated along the coastal front inversion (section 3d).

The turbulence undergoes a substantial reduction in amplitude as the air travels inland. This is to be expected, since the marine layer undergoes a transition from a neutrally stratified boundary layer to a weakly stratified elevated layer. Offshore, the spectra of all four atmospheric variables are nearly flat and only weakly coherent, with no notable peaks in the spectra. In the −25- to 2-km leg, the spectral density at smaller scales in the wind components has decreased by a factor of three, and an additional factor of 15 drop is found in the −50- to −25-km leg. The spectra of u and v, initially similar at all wavelengths, remain similar for wavelengths less than 1 km. Between 1- and 2-km wavelengths, the Kelvin–Helmholtz wave signature dominates the u power spectrum, while beyond 5 km the spectra may be influenced by changes in the vertical position of the aircraft relative to the frontal inversion.

In summary, the turbulence characterizing the marine boundary layer offshore decays rapidly as the air flows over the coastal front, and waves of 1 to 2 km become noticeable near −25 km. The phase structure and high coherence of these waves indicate the presence of waves on the inversion beneath the aircraft. Visual inspection of these waves (Fig. 3b) indicates that these waves are present at roughly constant amplitude throughout the range −30 to −50 km.

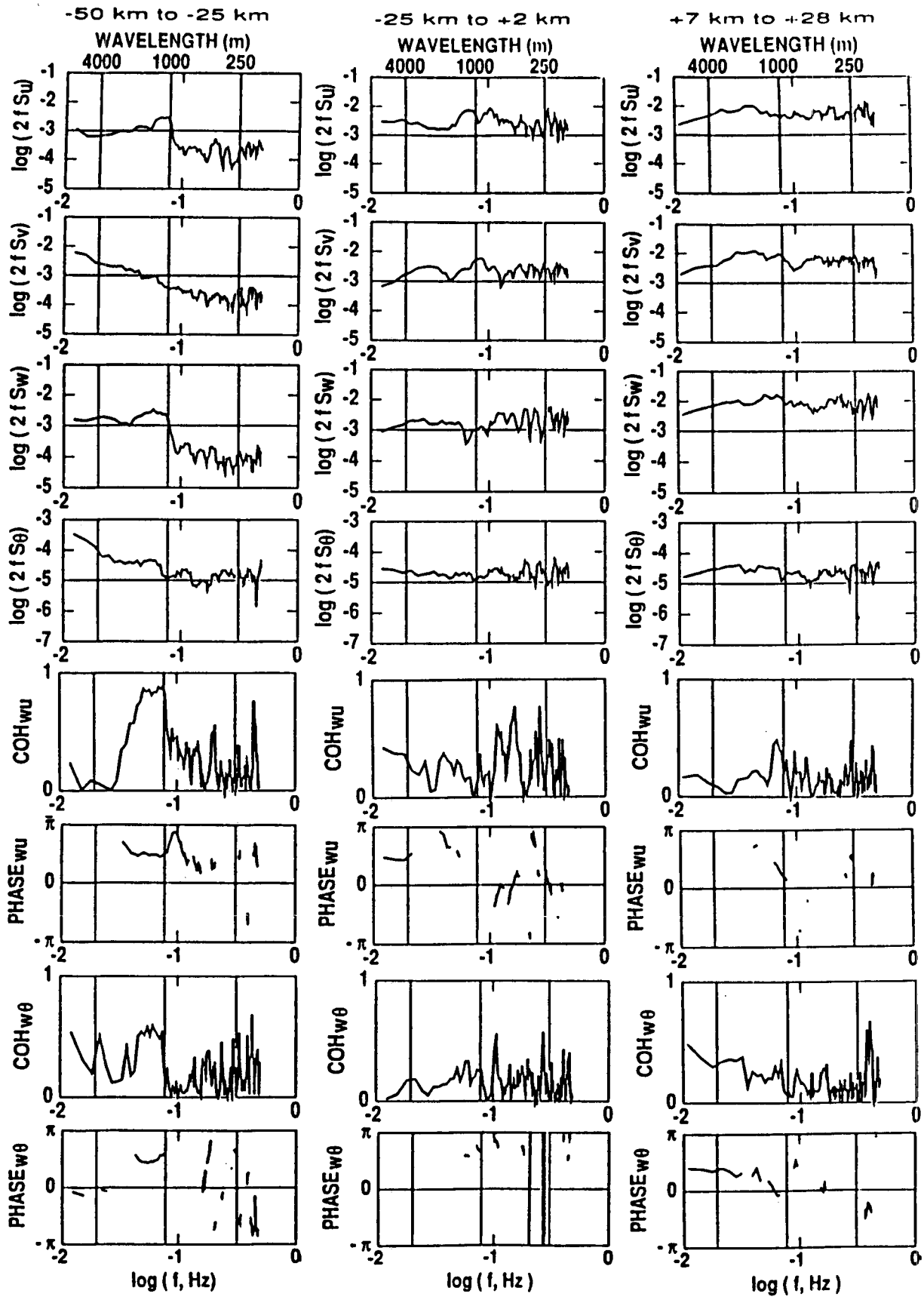
-50 km to -25 km
-25 km to +2 km
+7 km to +28 km
WAVELENGTH (m)
4000 1000 250
log (2fSu)
log (2fSv)
log (2fSw)
log (2fSθ)
COHwu
PHASEwu
COHwθ
PHASEwθ
log (f, Hz)

b. Billow signatures in pass 2

The ubiquity of the oscillations above the inversion implies that Kelvin–Helmholtz billows should be present within the inversion throughout the region −30 to −50 km. Judging from the temperature and wind records (Fig. 3) and the aircraft altitude (Fig. 1), the aircraft while on pass 2 descended through the inversion from −54.5 to −51.5 km, ascended through the inversion from −46 to −44.5 km, descended back into the inversion at −43 km, and remained within the inversion from −43 to −30.5 km. The search for Kelvin–Helmholtz billows will concentrate on the −43 to −30.5 km segment.

The high-amplitude waves present between −37 and −32.5 km were investigated in detail in section 3. Figure 4, while centered on the high-amplitude waves, also encompasses representative segments of data from before and after the waves. Between −32.5 and −31 km are parts of two waves with wavelength near 1.2 km, which appear to be at an earlier stage in their life cycle than the high-amplitude waves. Beyond −37 km there is an apparent lack of coherent structure, particularly in the potential temperature record, which shows rapid high-amplitude temperature swings that contrast sharply with the record between −32.5 and −31 km.

Numerical simulations of high Reynolds number Kelvin–Helmholtz instability (Klaassen and Peltier 1985) indicate that as the wave breaks, the vorticity and potential temperature become wrapped up within the cat's-eye vortex, but the cat's-eye circulation itself maintains its coherent structure. An aircraft horizontally traversing such billows should therefore pass through a smoothly varying vertical-motion structure (with some small-scale variations due to vorticity roll up) and a seemingly chaotic temperature structure. At that point in the wave where the vertical motion shifts from upward to downward, a nearly instantaneous rise in temperature should be observed corresponding to the so-called braid. The structure of the horizontal wind should depend strongly on the location of the aircraft relative to the steering level, but should otherwise remain as coherent as w.

To search for these structures between −37 and −43 km, we compare in Fig. 14 the complete 1-s resolution temperature data to wind data smoothed by an 8-s (approximately 500 m) running mean. Contiguous with the wave peak at −35.9 km, which was part of the wave train discussed in section 3c, there are broad maxima in both u and w near −37.6, −39.2, and −40.4 km. The u–w phase relationship is similar to that observed in the wave train, and the wavelengths are also similar. The temperature data show evidence of coherent structure near −40 km, but evidence of braids is inconclusive.

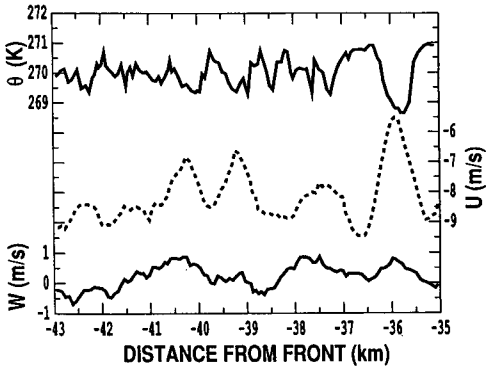

FIG. 14. Unsmoothed potential temperature (solid), smoothed front-normal wind (dashed), and smoothed vertical velocity (solid) for segment of pass 2 adjoining the high-amplitude waves. Smoothing was by an 8-point running mean.

Based on the coherence between u and w and the contiguity with the previously discussed wave train, it seems likely that the aircraft indeed passed through mature Kelvin–Helmholtz billows between −37 and −41 km, but the lack of consistency in the temperature record from wave to wave prevents any determination of wave structure other than wavelength.

Another possible pair of Kelvin–Helmholtz billows is suggested by the temperature and wind data from pass 2 between −16 and −25 km. Apparent aircraft passages through braids are present at −20 and −24.5 km. A spectral analysis of this data segment indicated little energy in w at the 4.5-km wavelength. Furthermore, w and θ were positively correlated at large wavelengths, implying that if these were billows, they were decaying.

6. Comparison with other NEWSEX coastal fronts

As described by NiNe, three other coastal fronts were systematically observed by aircraft during NEWSEX. Within this entire dataset, the aircraft flew within a total of approximately 100 km of coastal front inversion, and only one other set of large-amplitude temperature and wind oscillations similar to the pass 2 wave train were found. During one aircraft pass through the coastal front of 10 January 1983, a total of 2.5 wavelengths were observed (wavelength 2 km) at about −15 km behind the surface frontal position. Because there was significant shear in the alongfront wind, it is likely that the actual wavelength of these waves was close to 1.4 km if the waves were indeed oriented normal to the shear.

In only one other case (12 December 1983) did the aircraft fly passes at farther than −30 km from the surface front. Unfortunately, these passes did not in-

FIG. 13. Power spectra S_x, coherence spectra COH_{xy}, and phase spectra $PHASE_{xy}$ of selected variables as a function of frequency f, for three time series of aircraft data from over water or above the coastal front inversion. Phase spectra are only plotted at those frequencies for which the coherence is greater than 0.2. The approximate wavelength equivalents of selected frequencies are indicated by vertical lines.

clude a pass within the coastal front inversion, so a direct comparison with the circumstances of the pass 2 wave train cannot be made. However, a spectral analysis of the lowest pass above the inversion should show evidence of Kelvin–Helmholtz waves if such waves are present. Such an analysis was performed on the pass flown at 710 m between −50 and −20 km. A maximum coherence of 0.45 between u and w was found near 1-km wavelength, but it did not correspond to a local maximum in power density, and the phase angle was −150°. It thus appears that no high-amplitude Kelvin–Helmholtz instabilities were present on 12 December 1983 within 50 km of the surface front position.

The bulk Richardson number structures of the four coastal-front cases were also estimated by NiNe, using 3–4-km averages of wind and potential temperature along horizontal aircraft passes to eliminate aliasing by Kelvin–Helmholtz waves. Below the frontal inversions, three of the four cold-air layers possessed Richardson numbers typically less than 0.2. The calculated Richardson numbers for 4 December 1983 were higher, but we have seen (Fig. 2) that the Richardson number calculated directly from an aircraft sounding is also well below 0.2. Within the frontal inversions, bulk Richardson numbers tended to lie between 0.25 and 0.35. This agrees well with laboratory data of inversion structure after the decay of Kelvin–Helmholtz instability (Thorpe 1973) and is consistent with the inversion structure near the surface front having been determined by Kelvin–Helmholtz mixing at and behind the density current head (NiNe). Above the inversions, Richardson numbers were generally between 0.5 and 1. Overall, the Richardson number structures of the four coastal front cases were nearly indistinguishable from one another.

7. Discussion

Kelvin–Helmholtz instability in the atmosphere has been observed or inferred in many different contexts (Ludlam 1967; Simpson 1969; Metcalf and Atlas 1972; Hardy et al. 1973; Browning et al. 1973; Neff 1986), and the waves documented in the present paper do not extend the current body of knowledge regarding environmental configurations likely to support Kelvin–Helmholtz billows. However, the waves observed during pass 2 were sampled at the optimal time near maximum amplitude and prior to wave breaking, so as to produce dramatic periodic high-amplitude variations in temperature and horizontal wind in the aircraft data.

The two-dimensional pass 2 wave structure has been reconstructed using the aircraft data at the 400-m level. The resulting potential temperature analysis, over the same horizontal range as Fig. 4, is shown in Fig. 15. No correction has been made for the Doppler shift of the wavelengths, causing an effective horizontal compression in Fig. 15 of about 10%. The vertical structure of the waves and basic state has been inferred from other passes and aircraft soundings, with the phase structure following that of the most unstable mode in the linear analysis. The amplitude of the waves was taken to be 100 m, which is consistent with the observed vertical motion and the growth rate calculated from the instability analysis (section 4d). Depiction of the Kelvin–Helmholtz billows was guided by the numerical simulations of Sykes and Lewellen (1982) and Klaassen and Peltier (1985). Given the amplitude and inferred two-dimensional structure of the waves at any stage in their life cycle, the pass 2 data were used to estimate the stage in evolution of each wave from the asymmetry and other details of the potential temperature. The reconstruction was constrained to match the raw 1-s pass 2 aircraft data at every point. The result closely resembles a similar reconstruction performed with aircraft data on 100-m waves by Metcalf and Atlas (1972).

Although Kelvin–Helmholtz instability was shown to be the only linear normal-mode instability consistent with the observed waves, the horizontal wavelength of the most unstable mode using the only available complete observed vertical profile was a factor of 2 less than observed. Investigation of the dependence of the most unstable wavelength on the possible range of profile variations indicated that the wavelength was quite sensitive to the inversion and shear thicknesses. The different wavelengths observed on successive aircraft passes could be accounted for by a 13 m change in the half-thickness of the shear layer, holding the inversion thickness constant. This strong dependence suggests that, rather than comparing observed and theoretical

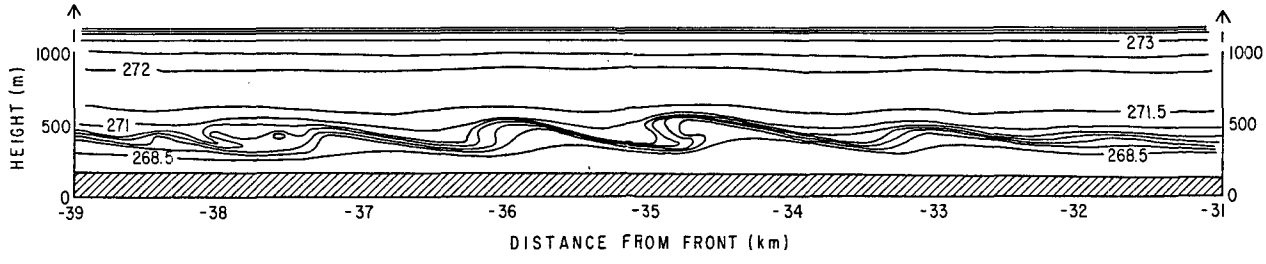

FIG. 15. Reconstruction of two-dimensional pass 2 wave structure, using unsmoothed pass 2 flight-level data and knowledge of the basic state, the linear modal structure, and the structure of nonlinear Kelvin–Helmholtz billows. Lines of constant potential temperature are drawn at 0.5 K intervals from the ground to just above the base of the warm-front inversion near 1100 m.

wavelengths as a test of linear theory, a more appropriate use of theory might be to deduce the basic-state structure from the observed wavelengths.

The theoretical *e*-folding time for the observed waves was on the order of five minutes. Given the observed and theoretical phase speeds of about -7 to -8 m s^{-1}, this translates to a Lagrangian distance of 2.5 km, which is much too short for the waves to have been generated or triggered near the surface frontal position. This is consistent with the pass 3 observations, which show a maximum in wave activity in the 1–2-km range only beyond roughly -25 km. Thus, it appears that for the 4 December 1983 coastal front, there were at least the following three inversion regimes.

1) The vicinity of the surface front, where density current dynamics predominate and where Kelvin–Helmholtz billows are generated at the leading edge of the front (NiNe). The very low Richardson number at the leading edge allows a wide range of unstable waves to grow rapidly, and a cascade toward increasing wavelength may be expected, similar to the laboratory simulations of Koop and Browand (1979).

2) The region between -5 and -20 km, where the initial Kelvin–Helmholtz overturning has stabilized the inversion, producing a bulk Richardson number near 0.3 (NiNe).

3) The region beyond -20 km, where the Richardson number has been brought below 0.25 by external influences, to be discussed in the following. The gradual destabilization of the inversion allows a single dominant wavelength to grow to finite amplitude before wave breaking, accounting for the clean periodicity observed in the aircraft data.

Neglecting the possibility of unusual small-scale fluxes within the inversion (spectral analysis of the range -15 to -25 km in pass 2 indicated a weak downward heat flux at small scales, in agreement with expectations), changes in the bulk Richardson number across the front require changes in the shear and/or temperature difference across the inversion. A mechanism for increasing the shear across the inversion with increasing distance behind the coastal front is peculiar to cold-air damming situations: the constriction of the marine air as it flows over the cold dome and beneath the warm-frontal inversion. As discussed by NiNe, mass continuity and two-dimensionality require the marine-air wind speed to increase with distance behind the coastal front. This expected increase was observed in the present case; Fig. 3b indicates a velocity gradient (acceleration) of 1 m s^{-1}/10 km. Assuming the temperature difference and inversion depth remain constant and taking a typical wind difference across the inversion of 8–10 m s^{-1}, the observed gradient would reduce Ri from 0.3 to 0.2 in a distance of 20 km, consistent with the observed variation in Kelvin–Helmholtz wave activity.

Although the acceleration of the marine air above the inversion appears to be sufficient to account for the onset of Kelvin–Helmholtz instability in the present case, other mechanisms are available. The most common ones are likely to be diurnal insolation, which would reduce the temperature difference across the inversion, and increasing onshore flow, which would increase the wind shear. To produce waves along the inversion, these changes must occur rapidly; the mixing at the head of the coastal front is constantly acting to hold the Richardson number behind the head at a stable value.

Kelvin–Helmholtz mixing injects heat and momentum into the cold air, both of which would tend to make the cold air tend to flow over the blocking orography rather than remain stagnant. The downward transfer of momentum would also tend to cut off the supply of cold air to the coastal front, causing the front to retreat westward. Therefore, under circumstances favoring Kelvin–Helmholtz instability, blocking theories that do not consider mixing (e.g., Xu 1990) should tend to overestimate the amount of cold-air damming that can occur. Conversely, processes such as evaporative cooling or freezing precipitation, which are common to cold-air damming episodes (Forbes et al. 1987) and are known to favor cold-air damming by making the cold air more dense, should also act to encourage damming by increasing the Richardson number across the inversion and thereby inhibit vertical mixing.

The sudden onset of Kelvin–Helmholtz instability presents a challenge to the modeling of cold-air damming. For steady-state conditions, the observational evidence indicates that mixing should occur in the immediate vicinity of the coastal front and beyond some critical distance that depends on the height of the overlying warm-front inversion. Because the dynamics of cold-air damming also depends crucially on frictional forces (Bell and Bosart 1988), this appears to be an example of an atmospheric flow whose successful modeling depends critically on the parameterization or explicit representation of the vertical diffusion of momentum.

Acknowledgments. I would like to thank Peter Neilley, Lance Bosart, and Ronald Miller for their comments and suggestions, and all of the participants in NEWSEX for enabling the dataset to be collected. The drafting of figures was performed by Marilyn Peacock. A portion of this work was done while the author was affiliated with the Center for Meteorology and Physical Oceanography, Massachusetts Institute of Technology. This research was supported by National Science Foundation Grants ATM-8209375, ATM-8607132, and ATM-8805550.

REFERENCES

Axford, D. N., 1973: On an observation of turbulent waves on the tropopause surface. *Quart. J. Roy. Meteor. Soc.*, **99**, 438–449.

Bell, G. D., and L. F. Bosart, 1988: Appalachian cold-air damming. *Mon. Wea. Rev.*, **116**, 137–161.

Britter, R. E., and J. E. Simpson, 1978: Experiments on the dynamics of a gravity current head. *J. Fluid Mech.*, **88**, 223–240.

Browning, K. A., G. W. Bryant, J. R. Starr, and D. N. Axford, 1973: Air motion within Kelvin–Helmholtz billows determined from simultaneous Doppler radar and aircraft measurements. *Quart. J. Roy. Meteor. Soc.*, **99,** 608–618.

——, T. W. Harrold, and J. R. Starr, 1970: Richardson number limited shear zones in the free atmosphere. *Quart. J. Roy. Meteor. Soc.*, **97,** 280–299.

Busack, B., and B. Brummer, 1988: A case study of Kelvin–Helmholtz waves within an off-shore stable boundary layer: Observations and linear theory. *Bound.-Layer Meteor.*, **5,** 29–41.

Davis, P. A., and W. R. Peltier, 1976: Resonant parallel shear instability in the stably stratified planetary boundary layer. *J. Atmos. Sci.*, **33,** 1287–1300.

De Baas, A. F., and A. G. M. Driedonks, 1985: Internal gravity waves in a stably stratified boundary layer. *Bound.-Layer Meteor.*, **16,** 303–323.

Droegemeier, K. K., and R. B. Wilhelmson, 1987: Numerical simulation of thunderstorm outflow dynamics. Part I: Outflow sensitivity experiments and turbulence dynamics. *J. Atmos. Sci.*, **44,** 1180–1210.

Forbes, G. S., R. A. Anthes, and D. W. Thomson, 1987: Synoptic and mesoscale aspects of an Appalachian ice storm associated with cold-air damming. *Mon. Wea. Rev.*, **115,** 564–591.

Fritts, D. C., and P. K. Rastogi, 1985: Convective and dynamical instabilities due to gravity wave motions in the lower and middle atmosphere: Theory and observations. *Radio Sci.*, **20,** 1247–1277.

Hardy, K. R., R. J. Reed, and G. K. Mather, 1973: Observation of Kelvin–Helmholtz billows and their mesoscale environment by radar, instrumented aircraft, and a dense rawinsonde network. *Quart. J. Roy. Meteor. Soc.*, **99,** 279–293.

Hazel, P., 1972: Numerical studies of the stability of inviscid stratified shear flows. *J. Fluid Mech.*, **51,** 39–61.

Holmboe, J., 1962: On the behavior of symmetric waves in stratified shear layers. *Geofys. Publ.*, **24,** 67–113.

Howard, L. N., 1961: Note on a paper of John W. Miles. *J. Fluid Mech.*, **10,** 509–512.

Jenkins, G. M., and D. G. Watts, 1968: *Spectral Analysis and its Applications.* Holden-Day, 525 pp.

Klaassen, G. P., and W. R. Peltier, 1985: Evolution of finite amplitude Kelvin–Helmholtz billows in two spatial dimensions. *J. Atmos. Sci.*, **42,** 1321–1339.

Koop, C. G., and F. K. Browand, 1979: Instability and turbulence in a stratified fluid with shear. *J. Fluid Mech.*, **93,** 135–159.

Lalas, D. P., and F. Einaudi, 1976: On the characteristics of gravity waves generated by atmospheric shear layers. *J. Atmos. Sci.*, **33,** 1248–1259.

Ludlam, F. H., 1967: Billow clouds and their relation to clear air turbulence. *Quart. J. Roy. Meteor. Soc.*, **93,** 419–435.

Merrill, J. T., 1977: Observational and theoretical study of shear instability in the airflow near the ground. *J. Atmos. Sci.*, **34,** 911–921.

Metcalf, J. I., and D. Atlas, 1972: Microscale ordered motions and atmospheric structure associated with thin echo layers in stably stratified zones. *Bound.-Layer Meteor.*, **4,** 7–35.

Miles, J. W., 1961: On the stability of heterogeneous shear flows. *J. Fluid Mech.*, **10,** 496–508.

——, and L. N. Howard, 1964: Note on a heterogeneous shear flow. *J. Fluid Mech.*, **20,** 331–336.

Neff, W. D., 1986: On the use of sodars to study stably stratified flow influenced by terrain. *Atmos. Res.*, **20,** 279–308.

Nielsen, J. W., 1989: The formation of New England coastal fronts. *Mon. Wea. Rev.*, **117,** 1380–1401.

——, and P. P. Neilley, 1990: The vertical structure of New England coastal fronts. *Mon. Wea. Rev.*, **118,** 1793–1807.

Patnaik, P. C., F. S. Sherman, and G. M. Corcos, 1976: A numerical simulation of Kelvin–Helmholtz waves of finite amplitude. *J. Fluid Mech.*, **73,** 215–240.

Rosenthal, A. J., and R. S. Lindzen, 1983: Instabilities in a stratified fluid having one critical level. Part II: Explanation of gravity wave instabilities using the concept of overreflection. *J. Atmos. Sci.*, **40,** 521–529.

Simpson, J. E., 1969: A comparison between laboratory and atmospheric density currents. *Quart. J. Roy. Meteor. Soc.*, **95,** 758–765.

Smyth, W. D., and W. R. Peltier, 1989: The transition between Kelvin–Helmholtz and Holmboe instability: An investigation of the overreflection hypothesis. *J. Atmos. Sci.*, **46,** 3698–3720.

Sykes, R. I., and W. S. Lewellen, 1982: A numerical study of breaking Kelvin–Helmholtz billows using a Reynolds-stress turbulence closure model. *J. Atmos. Sci.*, **39,** 1506–1520.

Thorpe, S. A., 1973: Experiments on instability and turbulence in a stratified shear flow. *J. Fluid Mech.*, **61,** 731–751.

Xu, Q., 1990: A theoretical study of cold air damming. *J. Atmos. Sci.*, **47,** 2969–2985.

Young, G. S., and R. H. Johnson, 1984: Meso- and microscale features of a Colorado cold front. *J. Climate Appl. Meteor.*, **23,** 1315–1325.